RSC Advances

PAPER

View Article Online
View Journal | View Issue

Cite this: *RSC Adv.*, 2020, **10**, 43273

Aliovalent-doped sodium chromium oxide ($Na_{0.9}Cr_{0.9}Sn_{0.1}O_2$ and $Na_{0.8}Cr_{0.9}Sb_{0.1}O_2$) for sodium-ion battery cathodes with high-voltage characteristics†

Woon Bae Park,‡[a] Muthu Gnana Theresa Nathan,‡[a] Su Cheol Han,[a] Jin-Woong Lee,[b] Kee-Sun Sohn *[b] and Myoungho Pyo *[a]

$NaCrO_2$ with high rate-capability is an attractive cathode material for sodium-ion batteries (NIBs). However, the amount of reversibly extractable Na^+ ions is restricted by half, which results in relatively low energy density for practical NIB cathodes. Herein, we describe aliovalent-doped O3–$Na_{0.9}[Cr_{0.9}Sn_{0.1}]O_2$ (NCSnO) and O3–$Na_{0.8}[Cr_{0.9}Sb_{0.1}]O_2$ (NCSbO), both of which show high-voltage characteristics that translate to an increase in energy density. In contrast to $NaCrO_2$, NCSnO and NCSbO can be reversibly charged to 3.80 and 3.95 V, respectively, delivering 0.5 Na^+ along with $Cr^{3+/4+}$ redox alone. The reversible chargeability to $Na_{0.4}[Cr_{0.9}Sn_{0.1}]O_2$ and $Na_{0.3}[Cr_{0.9}Sb_{0.1}]O_2$ is not associated with the suppression of Cr^{6+} formation. Both compounds show concentrations of Cr^{6+} that are higher than that of $Na_{0.3}CrO_2$, with an absence of O3′ phases. This implies that aliovalent-doping contributes to a suppression of the Cr^{6+} migration into tetrahedral sites in the interslab space, which reduces the possibility of irreversible comproportionation. NCSnO and NCSbO deliver capacities comparable to that of $NaCrO_2$, but show a higher average discharge voltage (2.94 V for $NaCrO_2$; 3.14 V for NCSnO; 3.21 V for NCSbO), which leads to a noticeable increase in energy densities. The high-voltage characteristics of NCSnO and NCSbO are also validated *via* density-functional-theory calculations.

Received 29th September 2020
Accepted 20th November 2020

DOI: 10.1039/d0ra08332a

rsc.li/rsc-advances

Introduction

With continuous expansion of the use of lithium-ion batteries (LIBs) as an almost unique power source for ubiquitous energy demands,[1,2] sustainability is becoming more and more important these days. One of the most promising solutions to this persistent issue for LIBs could be the development of sodium-ion batteries (NIBs), because sodium is plentiful in nature and has a reduction potential that is comparable to that of lithium.[3] Therefore, various Na-storage materials have been developed as NIB cathode candidates,[4–14] most of which are based on a layered structure. P2–$Na_{2/3}[Mg_{0.28}Mn_{0.72}]O_2$,[15] O3–$Na[Fe_{0.50}Co_{0.50}]O_2$,[16] and P3/P2/O3–$Na_{0.76}Mn_{0.5}Ni_{0.3}Fe_{0.1}Mg_{0.1}O_2$ (ref. 17) are only a few of the cathode materials with a high energy density of *ca.* 500 W h kg^{-1}.

The crystallographic structure and electrochemical properties of layered NIB cathodes are often compared to those of layered LIB cathodes because the fundamental chemistry of the former is similar to that of the latter. A slight difference in the ionic size of mobile ions (Li^+ = 0.76 Å *vs.* Na^+ = 1.02 Å), however, significantly affects the structural stability, which causes distinctively different phase-transition and voltage behaviors during charge/discharge (C/D). In general, large Na^+ ions tend to reside in a prismatic site rather than in an octahedral site, which induces multiple phase transitions with x variations during C/D in Na_xMO_2 (M = first-series transition metals). For example, while O3–$LiCoO_2$ is generally known to maintain its hexagonal structure up to $Li_{\sim 0.5}CoO_2$,[18–20] the O3 phase of $NaCoO_2$ is frequently changed to O′3 ($Na_{0.95}CoO_2$), P′3 ($Na_{0.9}CoO_2$), and P3 ($Na_{0.82}CoO_2$) during a charge process, which leads to inferior cyclic stability of O3–$NaCoO_2$ compared with that of O3–$LiCoO_2$.[13,21]

Another interesting example of the dramatic effect of ionic size is $NaCrO_2$. In contrast to O3–$LiCrO_2$, which suffers from the hindrance of Li^+ diffusion due to Cr^{6+} ions generated during charging,[22] O3–$NaCrO_2$ shows reversible Na^+ intercalation/de-intercalation within a reasonable voltage window.[22–31] Unless the high-voltage cutoff (E^{high}) exceeds *ca.* 3.6 V, the hexagonal O3 phase of $NaCrO_2$ is reversibly transformed to a monoclinic

[a]*Department of Printed Electronics Engineering, Sunchon National University, Chonnam 57922, Republic of Korea. E-mail: mho@sunchon.ac.kr*

[b]*Faculty of Nanotechnology and Advanced Materials Engineering, Sejong University, Seoul 05006, Republic of Korea. E-mail: kssohn@sejong.ac.kr*

† Electronic supplementary information (ESI) available: EDX results and Rietveld refinement fits for as-synthesized samples, and tables summarizing Rietveld refinement results for fully charged samples. See DOI: 10.1039/d0ra08332a

‡ These authors contributed equally to this work.

P′3 type *via* the monoclinic O′3 phase and delivers a capacity of *ca.* 120 mA h g^{-1} ($Na_{0.5}CrO_2$).[23–25] Further charging beyond 3.6 V results in the irreversible formation of another O3 phase (O3′) and a rock-salt structure with Cr^{6+} in tetrahedral sites and Cr^{4+} in octahedral sites between interslabs, respectively.[26,27] The E^{high} during C/D in $NaCrO_2$, therefore, is usually limited to 3.6 V to avoid a detrimental structure-transformation, which signifies that the voltage limitation must be solved to increase the energy density of $NaCrO_2$. To tackle this issue in $NaCrO_2$, Cr-based multi-metallic systems have been studied and possible increases in average operating voltage have been addressed.[32–35] For example, Cao *et al.* claimed that the disproportionation reaction can be effectively suppressed in $NaCr_{1/3}Fe_{1/3}Mn_{1/3}O_2$ due to the presence of Fe^{3+} and Mn^{4+} when charged to 4.2 V.[32] However, although $Cr^{3+/4+}$ redox is involved in these multi-metallic compounds, a significant fraction of electroactivity was the result of other metallic species, and the contribution from $Cr^{3+/4+}$ redox was not substantial. An effort aimed at structural stabilization by sodium-site doping with calcium has also been examined.[36,37]

In this work, we describe aliovalent doping and its effect of on the electrochemical behaviors in $NaCrO_2$ (O3–$Na_{0.9}[Cr_{0.9}Sn_{0.1}]O_2$ and O3–$Na_{0.8}[Cr_{0.9}Sb_{0.1}]O_2$), in which Sn^{4+} and Sb^{5+} ions are electrochemically inert and their fraction is relatively small, in contrast to previous studies. First, we evaluate the structural stability *via* density functional theory (DFT) calculation and find that $NaCrO_2$ with higher contents of Sn^{4+} and Sb^{5+} does not retain the O3 structure. We also experimentally demonstrate that the title compounds can be reversibly charged to voltages exceeding 3.6 V until 0.5 Na^+ is extracted (3.80 V in $Na_{0.4}[Cr_{0.9}Sn_{0.1}]O_2$ and 3.95 V in $Na_{0.3}[Cr_{0.9}Sb_{0.1}]O_2$), which results in a higher energy density than pristine $NaCrO_2$. The origin of the reversibility and the high-voltage features are discussed based on structural analysis and theoretical computation.

Experimental

All chemicals were purchased from Sigma-Aldrich unless otherwise mentioned. The O3–$NaCrO_2$ was synthesized *via* a conventional solid-state method reported elsewhere.[10] For the synthesis of O3–$Na_{0.9}[Cr_{0.9}Sn_{0.1}]O_2$ and O3–$Na_{0.8}[Cr_{0.9}Sb_{0.1}]O_2$, stoichiometric amounts of Na_2CO_3, Cr_2O_3, $CrSbO_4$, and SnO_2 were used as starting materials. $CrSbO_4$ was obtained by heating a mixture of Cr_2O_3 and Sb_2O_3 at 1100 °C for 12 h under an air atmosphere.[38] The precursors were mixed in a mortar and the mixture was pressed into pellets (5 wt% excess of Na_2CO_3 was used in order to compensate for Na loss at high temperature). The pellets were sintered at 750 °C for 3 h, and then at 1200 °C for 8 h under a continuous flow of Ar. The samples were naturally cooled and stored in an Ar-filled glove box until further use.

Ex situ X-ray diffraction (XRD) was carried out to identify the crystalline phases of the as-prepared powders as well as C/D cycled electrodes. The measurements were performed using an X-ray diffractometer (Rigaku ULTIMA 4) with monochromatic Cu K_α radiation (λ = 1.5406 Å). To prevent the exposure of samples to the atmosphere during XRD measurements, the samples were sealed in an air-sensitive holder covered with Kapton film. The XRD patterns of pristine powders and electrochemically charged films were characterized *via* Rietveld refinement using FullProf software. The surface morphologies and the compositions of the synthesized compounds were examined using a JEOL JSM-7100F field emission scanning electron microscope (FESEM) and energy dispersive X-ray (EDX). A Thermo Fisher X-ray photoelectron spectrometer (XPS) with an Al K_α X-ray source was used to investigate the chemical state of chromium.

To prepare the electrodes, active material (80 wt%), acetylene black (10 wt%), and polyvinylidene fluoride (10 wt%) were mixed with *N*-methyl-2-pyrrolidone. The slurry was pasted onto Al foil using a doctor blade and was then vacuum-dried at 100 °C for 2 h. The electrodes were cut into a circular disk with a diameter of 16 mm. The typical mass loading of active material was *ca.* 2 mg cm^{-2}. For electrochemical tests, 2032 coin-type half-cells were fabricated in an Ar-filled glove box using Na metal as a counter/reference electrode, a separator (Whatman glass filter), and 1 M $NaPF_6$ dissolved in ethylene carbonate : diethyl carbonate (EC : DEC, 1 : 1) as electrolytes. Galvanostatic C/D tests were carried out using a WonATech (WBCS 3000) battery tester.

Result and discussion

In this study, we selected Sn^{4+} and Sb^{5+} ions for aliovalent doping of O3–$NaCrO_2$ because of the similarity in the ionic radii ($r[Cr^{3+}]$ = 0.615, $r[Sn^{4+}]$ = 0.69, and $r[Sb^{5+}]$ = 0.60 Å) and the possession of the highest oxidation states, in which the latter ensures electrochemical inertness during a high-voltage charge. We first compared the structural stabilities of $Na_{1-x}[Cr_{1-x}Sn_x]O_2$ and $Na_{1-2x}[Cr_{1-x}Sb_x]O_2$ in different phases (O3, P2, and P3) *via ab initio* DFT calculation. The total energies (E_T) for O3, P2, and P3 were calculated using $R\bar{3}m$, $P6_3/mmc$, and $R3m$ space groups, respectively. The 3 × 2 × 1 (O3 and P3) and 3 × 3 × 1 (P2) supercells, which contain the same number of formula units (18 units), were used to estimate the possible configurations for each composition (*i.e.*, $Na_{16}[Cr_{16}Sn_2]O_{36}$ for x = 0.1; $Na_{14}[Cr_{14}Sn_4]O_{36}$ for x = 0.2; $Na_{13}[Cr_{13}Sn_5]O_{36}$ for x = 0.3; $Na_{14}[Cr_{16}Sb_2]O_{36}$ for x = 0.1; $Na_{12}[Cr_{15}Sb_3]O_{36}$ for x = 0.15; $Na_{10}[Cr_{14}Sb_4]O_{36}$ for x = 0.2). The total number of configurations for each composition was checked using a supercell program developed by Okhotnikov *et al.*[39] Among them, we randomly selected 10 configurations for each composition, which appeared to be distinctive from each other and to be entropically plausible.

DFT calculations were executed using the Vienna *ab initio* simulation package (VASP5.3),[40] in which a GGA-PBE (generalized gradient approximation parameterized by Perdew, Burke, and Ernzerhof) exchange correlation functional,[41] a PAW (projector-augmented-wave) potential with an energy cutoff of 500 eV,[42,43] and a 3 × 3 × 2 *k*-mesh determined by the Monkhorst–Pack scheme were implemented.[44] The atomic position and lattice size were allowed to relax until the total energy accuracy and ionic force components converged to 10^{-5} eV and

0.01 eV Å^{-1}, respectively. The on-site interaction (Hubbard U) value was set to 4.0 for a Cr d orbital.[45]

The E_T values for each composition with different structures, as compared in Fig. 1, clearly show that the most stable structure strongly depends on the composition. For example, the average E_T value of −24.94 eV per FU for the O3 type of $Na_{0.8}[Cr_{0.9}Sb_{0.1}]O_2$ was appreciably lower than the −24.83 eV per FU for either P2 or P3 types. The O3 preference was also the case in $Na_{0.9}[Cr_{0.9}Sn_{0.1}]O_2$. The stability of $Na_{0.8}[Cr_{0.9}Sb_{0.1}]O_2$ and $Na_{0.9}[Cr_{0.9}Sn_{0.1}]O_2$, therefore, indicated that the O3 structure could be stable in a wide range of Na^+ content after aliovalent substitution in contrast to the brief existence of an O3 phase in $NaCrO_2$ during charge.[23–27] Further increases in the amounts of substituents (Sn^{4+} and Sb^{5+}), and thereby a decrease in the content of Na^+, changed the most stable phase to a P2 type, but the energetic preference over O3 was not so conspicuous as that for $Na_{0.9}[Cr_{0.9}Sn_{0.1}]O_2$ and $Na_{0.8}[Cr_{0.9}Sb_{0.1}]O_2$.

$Na_{0.9}[Cr_{0.9}Sn_{0.1}]O_2$ (NCSnO) and $Na_{0.8}[Cr_{0.9}Sb_{0.1}]O_2$ (NCSbO), which were predicted to retain the O3 structures in DFT calculations, were synthesized *via* a conventional solid-state method and subjected to XRD measurements along with pristine O3–$NaCrO_2$ (NCO) (Fig. 2). We selected these two compounds because the goal of this research was to investigate the effect of aliovalent doping on the electrochemical behaviors of O3–NCO when $Cr^{3+/4+}$ alone is involved in a redox process. *Ex situ* XRD revealed the formation of O3 layered structures in both NCSnO and NCSbO in accordance with the DFT results. The characteristic peaks of O3 phases (space group = $R\bar{3}m$) were evident with small impurities (Na_2CrO_4 denoted by asterisks). The most intense (003) and (104) peaks showed well-defined symmetric shapes with neither peak-splitting nor shoulders, which indicated the absence of monoclinically distorted phases (O′3, space group = $C2/m$) in as-prepared compounds. The negligible peak intensities of (015) relative to (104) also suggested that Na^+ ions resided in the octahedral sites (*i.e.*, no P3 or P′3 phases) for all compounds. It was also obvious that the *c*-axis length increased with the incorporation of Sn^{4+} or Sb^{5+} because of a decrease in Na^+ content with a concomitant increase in electrostatic repulsion between the MO_6 layers. The (003) peak located at 16.62° in NCO was shifted to lower 2θ angles of 16.34° and 16.28° in NCSnO and NCSbO, respectively. This also implied that Sn^{4+} and Sb^{5+} ions were unlikely to occupy the octahedral sites in Na^+ layers; otherwise, the *c*-axis lengths could be shortened in NCSnO and NCSbO. An increase in the relative intensities of (101)/(012) after substitution was another indication for the existence of Sn^{4+} and Sb^{5+} in the transition metal layers.

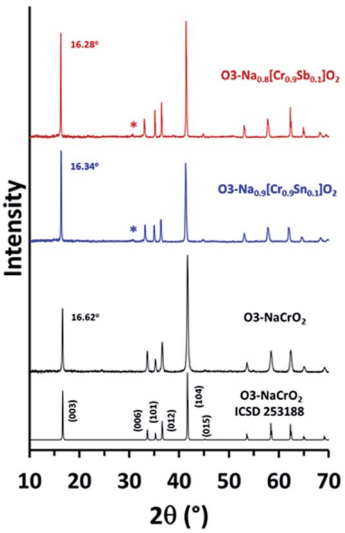

Fig. 2 Comparison of the *ex situ* XRD patterns of NCO, NCSnO, and NCSbO. Asterisks indicate a small impurity phase (Na_2CrO_4).

Prior to the extraction of detailed crystallographic information *via* Rietveld refinement, EDX studies were performed to confirm the chemical composition of as-synthesized compounds (Fig. S1†). FESEM images showed no morphological changes after substitutions with Sn^{4+} and Sb^{5+}.[46,47] The particles retained platelet shapes, which reflected the characteristic morphology of layered materials. The corresponding elemental maps also showed a homogeneous distribution of individual elements. The EDX spectra revealed the compositions of $Na_{0.89\pm0.02}Cr_{0.91\pm0.02}Sb_{0.09\pm0.01}O_2$ and $Na_{0.80\pm0.02}Cr_{0.91\pm0.02}Sb_{0.09\pm0.00}O_2$ for NCSnO and NCSbO, respectively, which indicated that the final compositions agreed well with the nominal compositions.

The change in the lattice parameters and atomic positions after aliovalent doping was estimated *via* Rietveld refinement (Fig. S2†). The positions of Na^+ and Cr^{3+} (Sn^{4+}, Sb^{5+}) were fixed at special sites. Only the *z* coordinate of O^{2-} was refined. The possibility for a site disorder between Na^+ and Cr^{3+} (Sn^{4+}, Sb^{5+}) was excluded because the simulated profiles deviated substantially from the XRD patterns, particularly at relative intensities of (006)/(101). Excellent agreement between the experimental and calculated patterns was obtained using the space group of $R\bar{3}m$ for all compounds (Table 1). The refinement results indicated that the interslab distance ($d_{interslab}$) was slightly increased after substitution, which was due to the enhanced electrostatic repulsion between MO_6 layers. In fact, the thickness of the Na^+ layers was significantly increased from 3.069 Å (NCO) to 3.168 (NCSnO) and 3.186 Å (NCSbO), but the

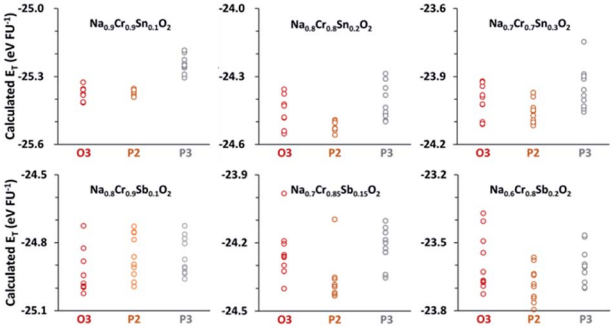

Fig. 1 Calculated E_T values per formula unit for various compositions with O3, P2, and P3 structures. Based on the average E_T values, the O3 structure proved to be the most plausible phase in both $Na_{0.9}Cr_{0.9}Sn_{0.1}O_2$ and $Na_{0.8}Cr_{0.9}Sb_{0.1}O_2$.

Table 1 Lattice parameters, fractional atomic coordinates, and isotropic thermal factor (U) obtained *via* Rietveld refinement for three compounds. Fractional (x y) coordinates for all atoms were fixed at (0 0)[a]

		$NaCrO_2$		$Na_{0.9}[Cr_{0.9}Sn_{0.1}]O_2$		$Na_{0.8}[Cr_{0.9}Sb_{0.1}]O_2$	
Atom	Wyckoff symbol	z/c	U (Å^2)	z/c	U (Å^2)	z/c	U (Å^2)
Na^+	3*b*	0.5	0.0091 (10)	0.5	0.0055 (12)	0.5	0.0052 (14)
Cr^{3+}	3*a*	0	0.0140 (7)	0	0.0053 (6)	0	0.0052 (10)
Sn^{4+}	3*a*			0	0.0053 (6)		
Sb^{5+}	3*a*					0	0.0052 (10)
O^{2-}	6*c*	0.2627 (2)	0.0007 (9)	0.2649 (2)	0.0056 (13)	0.265 (2)	0.0067 (13)

[a] Space group: $R\bar{3}m$; number of formula per unit cell (z) = 3; $NaCrO_2$: a = 2.977727 (4) Å, c = 15.9805 (5) Å, R_p = 2.82, R_{wp} = 3.68, R_{exp} = 1.92 and χ^2 = 3.68; $Na_{0.9}[Cr_{0.9}Sn_{0.1}]O_2$: a = 2.9833 (1) Å, c = 16.1285 (5) Å, R_p = 4.96, R_{wp} = 7.00, R_{exp} = 4.37 and χ^2 = 2.57; $Na_{0.8}[Cr_{0.9}Sb_{0.1}]O_2$: a = 2.9735 (1) Å, c = 16.1993 (7) Å, R_p = 4.65, R_{wp} = 6.31, R_{exp} = 4.37 and χ^2 = 2.09.

simultaneous contraction in the thickness of MO_6 layers (2.258 Å for NCO → 2.208 Å for NCSnO and 2.214 Å for NCSbO) resulted in relatively small changes in $d_{interslab}$ (Fig. 3). The volumes of MO_6 octahedra in both NSCnO and NCSbO (11.343 and 11.302 Å^3) were also slightly smaller than that in NCO (11.557 Å^3), despite the inclusion of larger cations in NCSnO.

The title compounds along with NCO were subjected to galvanostatic C/D at 20 mA g^{-1} to examine how the substitution influenced to the voltage behaviors (Fig. 4). As well known, NCO showed the good reversibility when the E^{high} is limited to 3.60 V with a charge capacity of 122 mA h g^{-1} ($Na_{\sim 0.5}CrO_2$).[23–25] An increase in the E^{high} to 3.90 V resulted in serious decay in the corresponding discharge capacity due to the formation of O3′ and/or rock-salt phases.[26,27] The charge profiles of NCSnO and NCSbO also indicated that $Na_{0.5}MO_2$ can be attained by charging to *ca.* 3.6 V with capacities of 97 and 77 mA h g^{-1}, respectively. The sharp increase of the voltages in NCO, however, were substantially alleviated in NCSnO and NCSbO, which indicated that the presence of immobile Sn^{4+} and Sb^{5+} hinders the charge re-distribution (Na^+/vacancy ordering) within MO_6 layers. Interestingly, further increases of E^{high} were possible to allow a reversible capacity of *ca.* 120 mA h g^{-1} (*i.e.*, $Na_{0.4}[Cr_{0.9}Sn_{0.1}]O_2$ and $Na_{0.3}[Cr_{0.9}Sb_{0.1}]O_2$) with no negative impact on the subsequent discharge process. As Fig. 4 (dotted lines) shows, by charging to 3.80 (NCSnO) and 3.95 V (NCSbO), *ca.* 0.5 Na^+ could be reversibly extracted. A subsequent discharge profile showed the retention of high-voltage characteristics *via* the delivery of *ca.* 50–60% of the total discharge capacity above 3.0 V. This implies that the charge process at voltages higher than 3.60 V in NCSnO and NCSbO was not ascribed to kinetic limitations (*i.e.*, overpotential). Instead, it was caused by the intrinsically high equilibrium potentials. Although NCSnO and NCSbO were stable up to 3.80 and 3.95 V, however, further charge resulted in a significant loss of reversibility. Fig. 4 (solid lines) shows that discharge capacities were reduced to 74 and 54 mA h g^{-1} after charging to 3.95 and 4.05 V in NCSnO and NCSbO, respectively. It is of note that the reversible capacities were not noticeably varied with mass loading in a range of 1.5 and 4.0 mg cm^{-2}, in contrast to sensitive dependance in $LiFePO_4$.[48,49]

In order to understand the reversibility of NCSnO and NCSbO within a wider potential window, we compared the oxidation states of chromium for fully charged NCSnO and NCSbO with those in NCO (Fig. 5). XPS spectra revealed that, while NCO charged to 3.60 V ($Na_{\sim 0.5}CrO_2$) contains negligible amounts of Cr^{6+}, the Cr^{6+} content is substantial in NCO charged to 3.80 V ($Na_{\sim 0.3}CrO_2$) due to the disproportionation of Cr^{4+}. The intense Cr^{6+} peak in $Na_{\sim 0.3}CrO_2$, however, became weaker again in NCO charged to 3.90 V ($Na_{\sim 0.2}CrO_2$), because of the comproportionation reaction to a rock-salt structure ($Cr_{Na+layer}^{6+} + 2Cr_{MO_6\ layer}^{3+} \rightarrow 3Cr_{rock\text{-}salt}^{4+}$).[26] In contrast, fully charged NCSnO and NCSbO ($Na_{0.4}[Cr_{0.9}Sn_{0.1}]O_2$ and $Na_{0.3}[Cr_{0.9}Sb_{0.1}]O_2$) showed strong Cr^{6+} peaks, which implied that the presence of Sn^{4+} and Sb^{5+} had not hampered the close proximity of Cr^{4+} ions for a disproportionation reaction ($3Cr_{MO_6\ layer}^{4+} \rightarrow Cr_{MO_6\ layer}^{6+} + 2Cr_{MO_6\ layer}^{3+}$). Despite the high concentration of Cr^{6+} in fully charged NCSnO and NCSbO, therefore, the electrochemical reversibility appeared to be maintained due to the

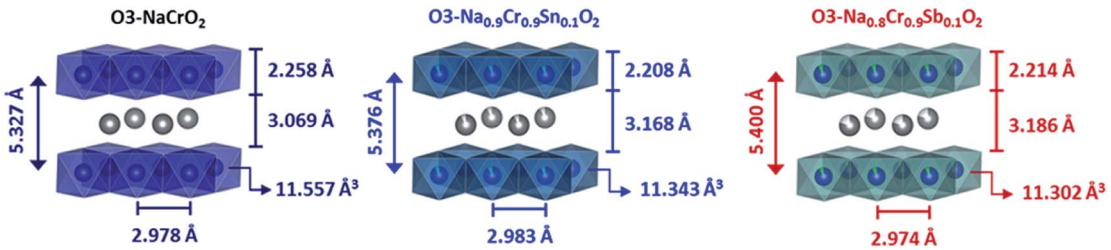

Fig. 3 Comparison of the structural features of NCO, NCSnO, and NCSbO.

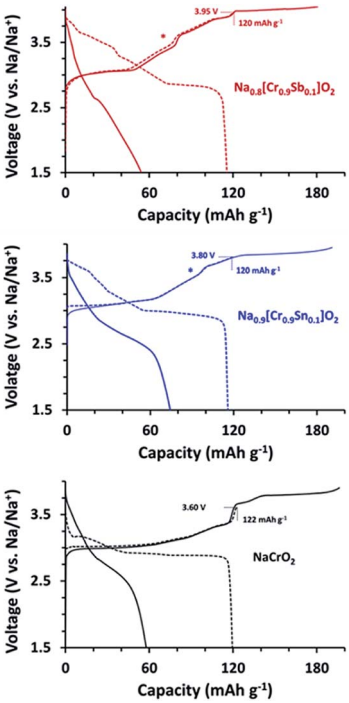

Fig. 4 1st C/D profiles of NCO, NCSnO, and NCSbO at 20 mA g^{-1} with different E^{high} values. (dotted line) E^{high} = 3.60, 3.80, and 3.95 V and (solid line) E^{high} = 3.90, 3.95, and 4.05 V for NCO, NCSnO, and NCSbO, respectively. Asterisks indicate the phase transition region at *ca.* 0.5 Na^+ in NCSnO and NCSbO, which is less pronounced than that in NCO.

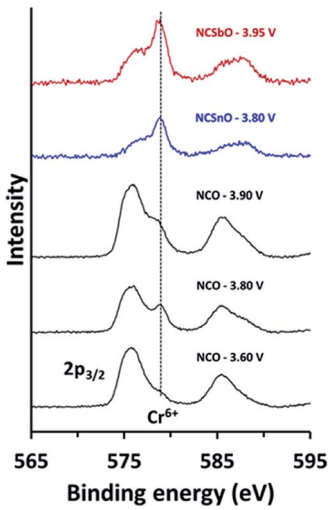

Fig. 5 High-resolution XPS on chromium for NCO, NCSnO, and NCSbO, charged to different voltages.

prevention of Cr^{6+} migration into the Na^+ layers, which is the route for the irreversible formation of O3′ and/or rock-salt phases.

Since the electrochemical reversibility of NCSnO and NCSbO with high E^{high} is not ascribed to the suppression of Cr^{6+} formation, we investigated the difference in the structural evolution to understand the high-voltage features of the two compounds. *Ex situ* XRD patterns during charge were recorded at various states-of-charge with an interval of 0.1 in Na^+ content. For NCO, the change in the XRD patterns agreed well with the previously reported results (Fig. 6A). On charging, (003) and (006) peaks of an O3 phase were split with a new peak appearing at a lower 2θ. Two separated peaks were observed in 0.9 Na^+ that immediately merged into a single peak when further charged to 0.8 Na^+ and 0.7 Na^+. Note that the (104) peak in the O3 phase was also split into two peaks with substantial intensities ((111) and (20-2)), which is a signature for the formation of a monoclinically distorted O′3 phase. Therefore, the change in the XRD patterns indicated a phase transition from O3 to O′3 through a mixed O3/O′3 phase when NCO was charged to $Na_{0.7}CrO_2$. The O′3 phase was immediately transformed to a P′3 phase with a further charge, which was evident from the abrupt weakening of the (111) and (20-2) peaks of O′3 and the appearance of intense (201) and (11-2) peaks of P′3 in a 2θ range of 44° and 45.5°. In appearance, the P′3 phase seemed to be maintained up to $Na_{0.3}CrO_2$ (charge to 3.80 V).

NCSnO and NCSbO showed phase transition behaviors that were noticeably different from those of NCO (Fig. 6B and C). During a charge, the O3 phases were maintained up to $Na_{0.7}MO_2$. Separation of the (003) and (006) peaks became evident at $Na_{0.6}MO_2$ in contrast to the incipient appearance in NCO ($Na_{0.9}CrO_2$). Furthermore, the structure of the two phases in $Na_{0.6}MO_2$ seemed to be different from that in $Na_{0.9}CrO_2$. The

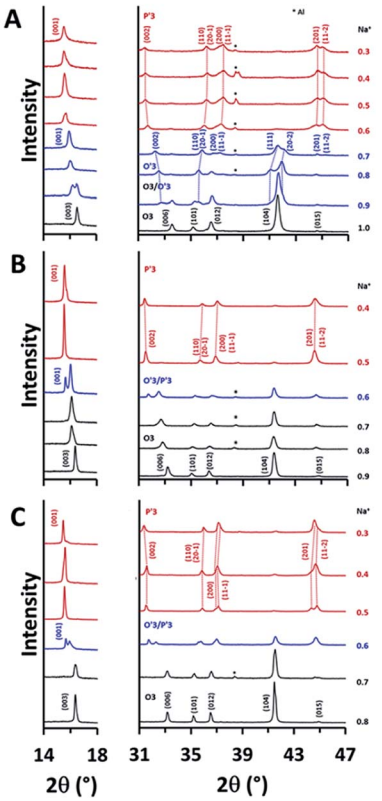

Fig. 6 Evolution of XRD patterns during Na^+ extraction in (A) NCO and (B) NCSnO with E^{high} of 3.80 V and (C) NCSbO with E^{high} of 3.95 V.

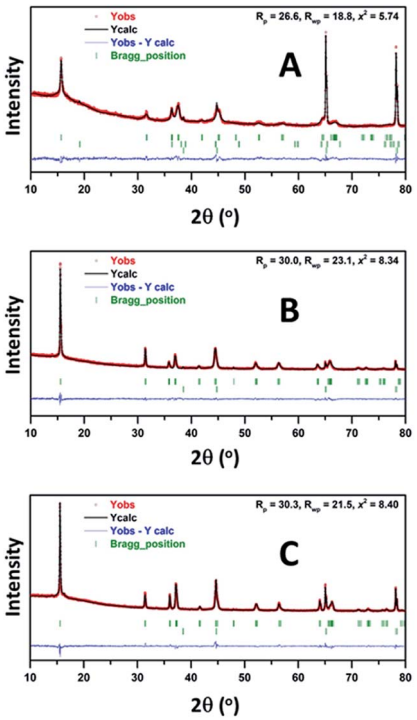

Fig. 7 Rietveld refinement of the XRD patterns for (A) $Na_{0.3}CrO_2$, (B) $Na_{0.4}[Cr_{0.9}Sn_{0.1}]O_2$, and (C) $Na_{0.3}[Cr_{0.9}Sb_{0.1}]O_2$ films. Experimental, calculated, and difference profiles are shown by the red dots, black line, and blue line, respectively. The green vertical tick marks above the difference profile denote the positions of Bragg reflections. (A) P′3–$Na_{0.4}CrO_2$, O3′–$Na_\delta CrO_2$, and Al (from the top); (B) P′3–$Na_{0.4}[Cr_{0.9}Sn_{0.1}]O_2$ and Al; (C) P′3–$Na_{0.3}[Cr_{0.9}Sb_{0.1}]O_2$ and Al.

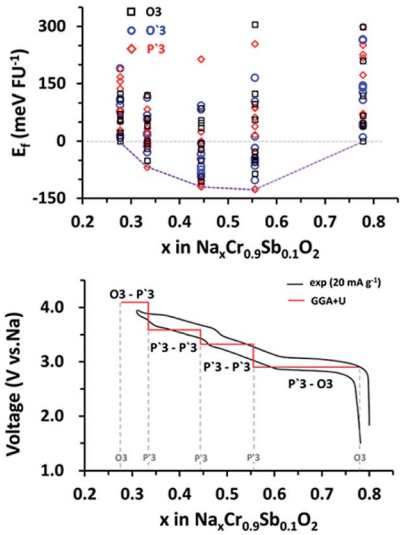

Fig. 8 (Top) Calculated values for the E_f of $Na_xCr_{0.9}Sb_{0.1}O_2$ as a function of Na^+ content (x = 0.28, 0.33, 0.44, 0.56, and 0.78). (Bottom) Calculated voltage profile (red) compared with the experimental C/D curve (black).

appreciable peak intensity at 2θ of *ca.* 44.7° strongly signified the inclusion of a P′3 phase. Despite no clear peak splitting, we also considered the presence of an O′3 phase in $Na_{0.6}MO_2$ from the peak broadening of (104). This two-phase region (O′3/P′3) was short-lived. It was immediately transformed to a P′3 phase, which was maintained to the fully charged states ($Na_{0.4}[Cr_{0.9}Sn_{0.1}]O_2$ and $Na_{0.3}[Cr_{0.9}Sb_{0.1}]O_2$).

It is noteworthy that, although all three compounds appeared to have the P′3 structures in a fully charged state ($Na_{0.3}CrO_2$, $Na_{0.4}[Cr_{0.9}Sn_{0.1}]O_2$, and $Na_{0.3}[Cr_{0.9}Sb_{0.1}]O_2$), closer examination revealed that, while $Na_{0.4}[Cr_{0.9}Sn_{0.1}]O_2$ and $Na_{0.3}[Cr_{0.9}Sb_{0.1}]O_2$ are composed of a single P′3 phase, $Na_{0.3}CrO_2$ contains O3′–$Na_\delta CrO_2$ along with P′3–$Na_{0.4}CrO_2$. The generation of O3′ and rock-salt structures in Na_xCrO_2 ($x < 0.4$), which led to irreversibility in Na^+ migration, was addressed in a previous report.[26] Our Rietveld refinement results also showed the presence of an O3′–$Na_\delta CrO_2$ between the experimental data and the calculated pattern by using a relative P′3–$Na_{0.4}CrO_2$/O3–$Na_\delta CrO_2$ ratio of 84.4/15.6. Note that the addition of rock-salt CrO_2 was avoided because of the strong diffraction peaks of an Al substrate, which closely overlapped those from rock-salt CrO_2. In contrast, the XRD patterns of $Na_{0.4}[Cr_{0.9}Sn_{0.1}]O_2$ and $Na_{0.3}[Cr_{0.9}Sb_{0.1}]O_2$ films were fitted well with a single P′3 phase and no O3′–$Na_\delta CrO_2$ (Fig. 7B, C, Tables S3 and S4†). Aliovalent doping, therefore, is likely to suppress the formation of O3′–$Na_\delta CrO_2$ in $Na_{0.4}[Cr_{0.9}Sn_{0.1}]O_2$ and $Na_{0.3}[Cr_{0.9}Sb_{0.1}]O_2$, which enables a charge to higher voltages in NCSnO and NCSbO.

The high-voltage characteristics of NCSbO were further validated *via* DFT calculations. The formation energy (E_f) was obtained for O3, O′3, and P′3 phases at various states-of charge, using 3 × 2 × 1, 3 × 2 × 1, and 1 × 3 × 3 supercells, respectively (Fig. 8). The electrochemical potential was calculated using the configuration with the lowest E_f for each x value. Eqn (1) was used, where $E(Na_{x1}Cr_{0.9}Sb_{0.1}O_2)$ and $E(Na_{x2}Cr_{0.9}Sb_{0.1}O_2)$ indicate the total energies of NCSbO with Na contents of $x1$ and $x2$, respectively. $E^{bulk}(Na)$ is the total energy of Na metal in a body-centered cubic ($Im\bar{3}m$) structure, which corresponds to the chemical potential of Na in the anode. F is the Faraday constant.

$$V = \frac{E(Na_{x1}Cr_{0.9}Sb_{0.1}O_2) - E(Na_{x2}Cr_{0.9}Sb_{0.1}O_2) + (x2 - x1)E^{bulk}(Na)}{(x2 - x1)F} \quad (1)$$

wherein one-third of Cr ions reside in the tetrahedral sites of Na^+ layers (Fig. 7A, Tables S1 and S2†). We obtained good agreement

The DFT-calculated voltage changes were well matched with the experimental C/D curves with the similar profile shapes and

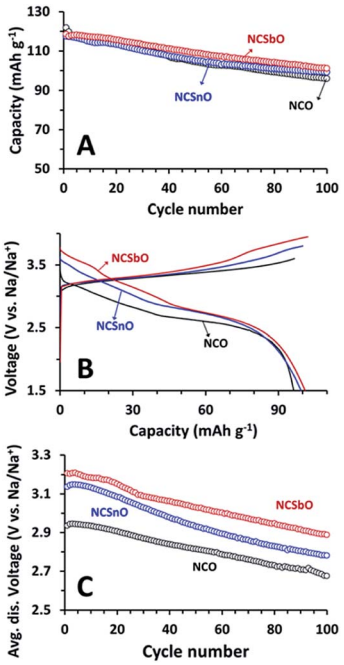

Fig. 9 (A) Discharge capacity retention, (B) representative voltage profiles (100th cycle), and (C) change in average discharge voltages of NCO, NCSnO, and NCSbO during galvanostatic C/D at 100 mA g^{-1}. Average discharge voltages were calculated by energy densities by the corresponding capacities. E^{high} = 3.60 V for NCO, 3.80 V for NCSnO, and 3.95 V for NCSbO.

voltage transitions, which validated the introduction of the high-voltage features by incorporating Sb^{5+} ions into NCO.

Finally, retention of the capacities and high-voltage characteristics of NCSnO and NCSbO were compared during 100 C/D cycles. With respect to the initial values, the capacities of NCSnO and NCSbO were gradually decreased with cycling, which was similar to the behavior of NCO (Fig. 9A). The degree of capacity fading was marginally different, showing fading rates of 0.26, 0.18, and 0.17 mA h g^{-1} $cycle^{-1}$ for NCO, NCSnO, and NCSbO, respectively. As a result, the capacities delivered after 100 C/D were comparable for three compounds (96 mA h g^{-1} for NCO, 99 mA h g^{-1} for NCSnO, and 101 mA h g^{-1} for NCSbO).

The high-voltage C/D properties of NCSnO and NCSbO were also maintained during 100 cycles. A comparison of the 100th voltage profiles revealed that, though the profile shapes were slightly distorted and the C/D voltages were lowered with respect to the 1st voltage profiles (Fig. 4), the high-voltage features in NCSnO and NCSbO were maintained (Fig. 9B). Indeed, the average discharge voltages were continuously decreased with cycling, but the relative superiority of NCSnO and NCSbO was not diminished (Fig. 9C). The average discharge voltages of 3.14 and 3.21 V during the 1st C/D for NCSnO and NCSbO were higher than that of NCO (2.94 V) by 0.20 and 0.27 V, respectively. These high-voltage features were maintained during 100 C/D cycles and resulted in the higher energy densities of NCSnO and NCSbO (275 and 292 mW g^{-1} *vs.* 263 mW g^{-1} for NCO after 100 cycles). We believe that, though not conspicuous (*ca.* 11% increase in NCSbO), the modification of reversible voltages and the increase of energy densities by electrochemically inert aliovalent doping in NCO suggest a new strategy to enhance the practicality of $NaCrO_2$ for use as a NIB cathode.

Conclusions

NCSnO and NCSbO, both of which retain an O3 structure, were synthesized and their electrochemical properties were examined in comparison to NCO. Despite a lower Na^+ content, NCSnO and NCSbO could reversibly intercalate/de-intercalate 0.5 Na^+ ($Na_{0.9}[Cr_{0.9}Sn_{0.1}]O_2 \leftrightarrow Na_{0.4}[Cr_{0.9}Sn_{0.1}]O_2$ and $Na_{0.8}[Cr_{0.9}Sb_{0.1}]O_2 \leftrightarrow Na_{0.3}[Cr_{0.9}Sb_{0.1}]O_2$) when charged to 3.80 and 3.95 V, respectively. The high-voltage characteristics were retained during subsequent discharge, showing average discharge voltages of 3.14 and 3.21 V for NCSnO and NCSbO, respectively, *vs.* 2.94 V for NCO. The higher C/D voltages of NCSnO and NCSbO were maintained during 100 C/D cycles with no impact on reversible capacities, which resulted in an improvement in energy density compared with that of NCO.

Elucidation of the high-voltage characteristics of NCSnO and NCSbO revealed that, although the aliovalent doping did not prevent the disproportionation of Cr^{4+} at a fully charged state, it hampered the formations of O3′–$Na_\delta CrO_2$ and/or rock-salt structures and enabled reversible Na^+ intercalation at voltages above 3.60 V. These experimental results were also validated *via* DFT calculation.

Conflicts of interest

There are no conflicts to declare.

Acknowledgements

This research was supported by Creative Materials Discovery Program through the NRF of Korea funded by the Ministry of Science, ICT and Future (2015M3D1A1069710), Basic Science Research Program (NRF-2014R1A6A1030419) and the NRF grant (2018R1C1B6006943), and the Technology Innovation Program (Alchemist Project, 20012196, Al based supercritical materials discovery) funded by the Ministry of Trade, Industry & Energy, Korea.

References

1 A. Mauger and C. M. Julien, Critical review on lithium-ion batteries: are they safe? sustainable?, *Ionics*, 2017, **23**, 1933–1947.
2 M. Sawicki and L. L. Shaw, Advances and challenges of sodium ion batteries as post lithium ion batteries, *RSC Adv.*, 2015, **5**, 53129–53154.
3 C. Delmas, Sodium and sodium-ion batteries: 50 years of research, *Adv. Energy Mater.*, 2018, **8**, 1703137.
4 Y. Niu, Y. Zhang and M. Xu, A review on pyrophosphate framework cathode materials for sodium-ion batteries, *J. Mater. Chem. A*, 2019, **7**, 15006–15025.

5 F. Sauvage, L. Laffont, J.-M. Tarascon and E. Baudrin, Study of the insertion/deinsertion mechanism of sodium into $Na_{0.44}MnO_2$, *Inorg. Chem.*, 2007, **46**, 3289–3294.

6 S. Xu, Y. Wang, L. Ben, Y. Lyu, N. Song, Z. Yang, Y. Li, L. Mu, H.-T. Yang, L. Gu, Y.-S. Hu, H. Li, Z.-H. Cheng, L. Chen and X. Huang, Fe-based tunnel-type $Na_{0.61}[Mn_{0.27}Fe_{0.34}Ti_{0.39}]O_2$ designed by a new strategy as a cathode material for sodium-ion batteries, *Adv. Energy Mater.*, 2015, **5**, 1501156.

7 M. Chen, W. Hua, J. Xiao, D. Cortie, X. Guo, E. Wang, Q. Gu, Z. Hu, S. Indris, X.-L. Wang, S.-L. Chou and S.-X. Dou, Understanding a new nasicon-type high voltage cathode material for high-power sodium-ion batteries, *Angew. Chem., Int. Ed.*, 2020, **59**, 2449–2456.

8 L. Bi, Z. Miao, X. Li, Z. Song, Q. Zheng and D. Lin, Improving electrochemical performance of $Na_3(VPO_4)_2O_2F$ cathode materials for sodium ion batteries by constructing conductive scaffold, *Electrochim. Acta*, 2020, **337**, 135816.

9 J. Li, X. He, S. Ostendorp, L. Zhang, X. Hou, D. Zhou, B. Yan, D. M. Meira, Y. Yang, H. Jia, G. Schumacher, J. Wang, E. Paillard, G. Wilde, M. Winter and J. Li, Tin modification of sodium manganese hexacyanoferrate as a superior cathode material for sodium ion batteries, *Electrochim. Acta*, 2020, **342**, 135928.

10 N. Naveen, W. B. Park, S. C. Han, S. P. Singh, Y. H. Jung, D. Ahn, K.-S. Sohn and M. Pyo, Reversible K^+-insertion/deinsertion and concomitant Na^+-redistribution in P′3-$Na_{0.52}CrO_2$ for high-performance potassium-ion battery cathodes, *Chem. Mater.*, 2018, **30**, 2049–2057.

11 Q. Liu, Z. Hu, M. Chen, C. Zou, H. Jin, S. Wang, S.-L. Chou and S.-X. Dou, Recent progress of layered transition metal oxide cathodes for sodium-ion batteries, *Small*, 2019, **15**, 1805381.

12 S. C. Han, E. G. Bae, H. Lim and M. Pyo, Non-crystalline oligopyrene as a cathode material with a high-voltage plateau for sodium ion batteries, *J. Power Sources*, 2014, **254**, 73–79.

13 S. J. R. Prabakar, J. Jeong and M. Pyo, Highly crystalline Prussian blue/graphene composites for high-rate performance cathodes in Na-ion batteries, *RSC Adv.*, 2015, **5**, 37545–37552.

14 S. Song, M. Kotobuki, Y. Chen, S. Manzhos, C. Xu, N. Hu and L. Lu, Na-rich layered $Na_2Ti_{1-x}Cr_xO_{3-x/2}$ ($x = 0$, 0.06): Na-ion battery cathode materials with high capacity and long cycle life, *Sci. Rep.*, 2017, **7**, 373.

15 N. Yabuuchi, R. Hara, K. Kubota, J. Paulsen, S. Kumakura and S. Komaba, A new electrode material for rechargeable sodium batteries: P2-type $Na_{2/3}[Mg_{0.28}Mn_{0.72}]O_2$ with anomalously high reversible capacity, *J. Mater. Chem. A*, 2014, **2**, 16851.

16 H. Yoshida, N. Yabuuchi and S. Komaba, $NaFe_{0.5}Co_{0.5}O_2$ as high energy and power positive electrode for Na-ion batteries, *Electrochem. Commun.*, 2013, **34**, 60–63.

17 M. Keller, D. Buchholz and S. Passerini, Layered Na-ion cathodes with outstanding performance resulting from the synergetic effect of mixed P- and O-type phases, *Adv. Energy Mater.*, 2016, **6**, 1501555.

18 H. Xia, L. Lu, Y. S. Meng and G. Ceder, Phase transitions and high-voltage electrochemical behavior of $LiCoO_2$ thin films grown by pulsed laser deposition, *J. Electrochem. Soc.*, 2007, **154**, A337–A342.

19 T. Ohzuku and A. Ueda, Solid-state redox reactions of $LiCoO_2$ ($R\bar{3}m$) for 4 volt secondary lithium cells, *J. Electrochem. Soc.*, 1994, **141**, 2972–2977.

20 W. G. Han, W. B. Park, S. P. Singh, M. Pyo and K.-S. Sohn, Determination of possible configurations for $Li_{0.5}CoO_2$ delithiated Li-ion battery cathodes via DFT calculations coupled with a multiobjective non-dominated sorting genetic algorithm (NSGA-III), *Phys. Chem. Chem. Phys.*, 2018, **20**, 26405–26413.

21 C. Delmas, J.-J. Braconnier, C. Fouassier and P. Hagenmuller, Electrochemical intercalation of sodium in Na_xCoO_2 bronze, *Solid State Ionics*, 1981, **3–4**, 165–169.

22 S. Komaba, C. Takei, T. Nakayama, A. Ogata and N. Yabuuchi, Electrochemical intercalation activity of layered $NaCrO_2$ vs. $LiCrO_2$, *Electrochem. Commun.*, 2010, **12**, 355–358.

23 S. Komaba, T. Nakayama, A. Ogata, T. Shimizu, C. Takei, S. Takada, A. Hokura and I. Nakai, Electrochemically reversible sodium intercalation of layered $NaNi_{0.5}Mn_{0.5}O_2$ and $NaCrO_2$, *ECS Trans.*, 2009, **16**, 43–55.

24 C.-Y. Chen, K. Matsumoto, T. Nohira, R. Hagiwara, A. Fukunaga, S. Sakai, K. Nitta and S. Inazawa, Electrochemical and structural investigation of $NaCrO_2$ as a positive electrode for sodium secondary battery using inorganic ionic liquid NaFSA–KFSA, *J. Power Sources*, 2013, **237**, 52–57.

25 Y.-N. Zhou, J.-J. Ding, K.-W. Nam, X. Yu, S.-M. Bak, E. Hu, J. Liu, J. Bai, H. Li, Z.-W. Fu and X.-Q. Yang, Phase transition behavior of $NaCrO_2$ during sodium extraction studied by synchrotron-based X-ray diffraction and absorption spectroscopy, *J. Mater. Chem. A*, 2013, **1**, 11130–11134.

26 S.-H. Bo, X. Li, A. J. Toumar and G. Ceder, Layered-to-rock-salt transformation in desodiated Na_xCrO_2 ($x < 0.4$), *Chem. Mater.*, 2016, **28**, 1419–1429.

27 K. Kubota, I. Ikeuchi, T. Nakayama, C. Takei, N. Yabuuchi, H. Shiiba, M. Nakayama and S. Komaba, New insight into structural evolution in layered $NaCrO_2$ during electrochemical sodium extraction, *J. Phys. Chem. C*, 2015, **119**, 166–175.

28 L. Liang, X. Sun, D. K. Denis, J. Zhang, L. Hou, Y. Liu and C. Yuan, Ultralong layered $NaCrO_2$ nanowires: a competitive wide-temperature-operating cathode for extraordinary high-rate sodium-ion batteries, *ACS Appl. Mater. Interfaces*, 2019, **11**, 4037–4046.

29 Y. Tsuchiya, A. M. Glushenkov and N. Yabuuchi, Effect of nanosizing on reversible sodium storage in a $NaCrO_2$ electrode, *ACS Appl. Nano Mater.*, 2018, **1**, 364–370.

30 Y. Wang, W. Li, G. Hu, Z. Peng, Y. Cao, H. Gao, K. Du and J. B. Goodenough, Electrochemical performance of large-grained $NaCrO_2$ cathode materials for Na-ion batteries synthesized by decomposition of $Na_2Cr_2O_7 \cdot 2H_2O$, *Chem. Mater.*, 2019, **31**, 5214–5223.

31 X. Xia and J. R. Dahn, $NaCrO_2$ is a fundamentally safe positive electrode material sfor sodium-ion batteries with liquid electrolytes, *Electrochem. Solid-State Lett.*, 2012, **15**, A1–A4.

32 M.-H. Cao, Y. Wang, Z. Shadike, J.-L. Yue, E. Hu, S.-M. Bak, Y.-N. Zhou, X.-Q. Yang and Z.-W. Fu, Suppressing the chromium disproportionation reaction in O3-type layered cathode materials for high capacity sodium-ion batteries, *J. Mater. Chem. A*, 2017, **5**, 5442–5448.

33 M. Cao, T. Wang, Z. Shadike, K. Nam, Y. Zhou and Z. Fu, Reversible multi-electron transfer of $Cr^{2.8+}/Cr^{4.4+}$ in O3-type layered $Na_{0.66}Fe_{1/3}Cr_{1/3}Ti_{1/3}O_2$ for sodium-ion batteries, *J. Electrochem. Soc.*, 2018, **165**, A565–A574.

34 M.-H. Cao, Z. Shadike, Y.-N. Zhou and Z.-W. Fu, Sodium-deficient O3-type $Na_{0.83}Cr_{1/3}Fe_{1/3}Mn_{1/6}Ti_{1/6}O_2$ as a new cathode material for Na-ion batteries, *Electrochim. Acta*, 2019, **295**, 918–925.

35 Y. Wang, P. Cui, W. Zhu, Z. Feng, M.-J. Vigeant, H. Demers, A. Guerfi and K. Zaghib, Enhancing the electrochemical performance of an O3–$NaCrO_2$ cathode in sodium-ion batteries by cation substitution, *J. Power Sources*, 2019, **435**, 226760.

36 L. Zheng, J. C. Bennett and M. N. Obrovac, Stabilizing $NaCrO_2$ by sodium site doping with calcium, *J. Electrochem. Soc.*, 2019, **166**, A2058–A2064.

37 S. C. Han, H. Lim, J. Jeong, D. Ahn, W. B. Park, K.-S. Sohn and M. Pyo, Ca-doped Na_xCoO_2 for improved cyclability in sodium ion batteries, *J. Power Sources*, 2015, **277**, 9–16.

38 M. G. T. Nathan, W. B. Park, N. Naveen, S. Park, K.-S. Sohn and M. Pyo, A Comparison of as-synthesized P2-$K_{0.70}[Cr_{0.85}Sb_{0.15}]O_2$ and ion-exchanged P2-$K_{0.62}Na_{0.08}[Cr_{0.85}Sb_{0.15}]O_2$ demonstrates the superiority of the latter as a potassium-ion battery cathode, *J. Electrochem. Soc.*, 2020, **167**, 100507.

39 K. Okhotnikov, T. Charpentier and S. Cadars, Supercell program: a combinatorial structure-generation approach for the local-level modeling of atomic substitutions and partial occupancies in crystals, *J. Cheminf.*, 2016, **8**, 17.

40 G. Kresse and J. Furthmüller, Efficient iterative schemes for ab initio total-energy calculations using a plane-wave basis set, *Phys. Rev. B: Condens. Matter Mater. Phys.*, 1996, **54**, 11169–11186.

41 J. P. Perdew, A. Ruzsinszky, G. I. Csonka, O. A. Vydrov, G. E. Scuseria, L. A. Constantin, X. Zhou and K. Burke, Restoring the density-gradient expansion for exchange in solids and surfaces, *Phys. Rev. Lett.*, 2008, **100**, 136406.

42 P. E. Blöchl, Projector augmented-wave method, *Phys. Rev. B: Condens. Matter Mater. Phys.*, 1994, **50**, 17953–17979.

43 G. Kresse and D. Joubert, From ultrasoft pseudopotentials to the projector augmented-wave method, *Phys. Rev. B: Condens. Matter Mater. Phys.*, 1999, **59**, 1758–1775.

44 H. J. Monkhorst and J. D. Pack, Special points for Brillouin-zone integrations, *Phys. Rev. B: Condens. Matter Mater. Phys.*, 1976, **13**, 5188–5192.

45 A. Jain, G. Hautier, S. P. Ong, C. J. Moore, C. C. Fischer, K. A. Persson and G. Ceder, Formation enthalpies by mixing GGA and GGA calculations, *Phys. Rev. B: Condens. Matter Mater. Phys.*, 2011, **84**, 045115.

46 B. Wang, B. Xu, T. Liu, P. Liu, C. Guo, S. Wang, Q. Wang, Z. Xiong, D. Wang and X. S. Zhao, Mesoporous carbon-coated $LiFePO_4$ nanocrystals co-modified with graphene and Mg^{2+} doping as superior cathode materials for lithium ion batteries, *Nanoscale*, 2014, **6**, 986–995.

47 T. Ruan, B. Wang, F. Wang, R. Song, F. Jin, Y. Zhou, D. Wang and S. Dou, Stabilizing the structure of $LiMn_{0.5}Fe_{0.5}PO_4$ via the formation of concentration-gradient hollow spheres with Fe-rich surfaces, *Nanoscale*, 2019, **11**, 3933–3944.

48 B. Wang, W. A. Abdulla, D. Wang and X. S. Zhao, A three-dimensional porous $LiFePO_4$ cathode material modified with a nitrogen-doped graphene aerogel for high-power lithium ion batteries, *Energy Environ. Sci.*, 2015, **8**, 869–875.

49 B. Wang, D. Wang, Q. Wang, T. Liu, C. Guo and X. Zhao, Improvement of the electrochemical performance of carbon-coated $LiFePO_4$ modified with reduced graphene oxide, *J. Mater. Chem. A*, 2013, **1**, 135–144.